Journal of Materials Science & Technology 153 (2023) 228–241

Contents lists available at ScienceDirect

Journal of Materials Science & Technology

journal homepage: www.elsevier.com/locate/jmst

Research Article

Chemical inhomogeneity inhibits grain boundary fracture: A comparative study in CrCoNi medium entropy alloy

Fuhua Cao[a,b], Yan Chen[a,b,*], Hai-Ying Wang[a,b], Lan-Hong Dai[a,b,c,*]

[a] State Key Laboratory of Nonlinear Mechanics, Institute of Mechanics, Chinese Academy of Sciences, Beijing 100190, China
[b] School of Engineering Science, University of Chinese Academy of Sciences, Beijing 101408, China
[c] School of Future Technology, University of Chinese Academy of Sciences, Beijing 100049, China

ARTICLE INFO

Article history:
Received 10 January 2023
Revised 1 February 2023
Accepted 10 February 2023
Available online 7 March 2023

Keywords:
Fracture
Chemical inhomogeneity
Grain boundary
Medium entropy alloy

ABSTRACT

Grain boundary (GB) fracture is arguably one of the most important reasons for the catastrophic failure of ductile polycrystalline materials. It is of interest to explore the role of chemical distribution on GB deformation and fracture, as GB segregation becomes a key strategy for tailoring GB properties. Here we report that the inhomogeneous chemical distribution effectively inhibits GB fracture in a model CoCrNi medium entropy alloy compared to a so-called 'average-atom' sample. Atomic deformation kinematics combined with electronic behavior analysis reveals that the strong charge redistribution ability in chemical disordered CrCoNi GBs enhances shear deformation and thus prevents GB crack formation and propagation. Inspects on the GBs with different chemical components and chemical distributions suggest that not only disordered chemical distribution but also sufficient "harmonic elements" with large electronic flexibility contribute to improving the GB fracture resistance. This study provides new insight into the influence mechanism of GB chemistry on fracture behavior, and yields a systematic strategy and criterion, from the atoms and electrons level, forward in the design of high-performance materials with enhanced GB fracture resistance.

1. Introduction

Grain boundaries (GBs) are essential defects for polycrystalline materials, playing a key role in the unexpected fracture of material by acting as preferential sites for damage nucleation and propagation. An intuitive example is the significant embrittlement of nanocrystalline metals characterized by a large volume fraction of GB regions [1–4]. GBs act as dislocation sources and sink simultaneously during plastic deformation, all of which can lead to damage and fracture at boundaries [5–10]. These GB-dislocation interaction induced GB damage and fracture are also responsible for stress corrosion cracking [11–13] and fatigue fracture [14,15] in metallic structural materials. Furthermore, the segregation of impurities on GB can often reduce the GB cohesion significantly and thus lead to intergranular brittleness [16–22]. Therefore, it is still of interest to study the GB fracture behavior of ductile metals, since GB damage happens in many service scenes. Abundant studies on the intergranular fracture mechanism elucidated that the ductile or brittle response of GB to crack propagation depends upon the GB misorientation [7,23,24], GB chemistry [25–28], GB complexion [17,29-31] and crack advance direction [32–34]. Ultimately, GB fracture is fundamentally atomistic in nature, manifested by the inability of GB atomic strains to be adequately accommodated by local atomic rearrangements.

As such, it is natural to propose that GBs with a strong ability to accommodate atomic strain are desired to restrain GB fracture. This idea has been substantiated by the fact that Cu/CuZr nanocrystalline-amorphous nanolaminates can exhibit superior tensile ductility than nanocrystalline Cu alone, which can be attributed to the high-capacity sinks for dislocation of the disordered amorphous intergranular film [35,36]. Impaired by these, Rupert and coauthors successfully improved the ductility of nanocrystalline Cu-Zr alloys to a high fracture strain of 56% by introducing amorphous intergranular films in GBs [2,37]. Recently, Wei et al. also found that amorphous ceramic grain boundaries in nanocrystalline nickel can coordinate deformation and thus improve plasticity of nanocrystalline nickel [38]. The finding that disordered GB structures can improve plasticity by delaying or preventing crack

* Corresponding authors.
E-mail addresses: chenyan@lnm.imech.ac.cn (Y. Chen), lhdai@lnm.imech.ac.cn (L.-H. Dai).

https://doi.org/10.1016/j.jmst.2023.02.002
1005-0302/

formation provides a new strategy to suppress GB fractures, which is promising for improving mechanical properties through GB engineering.

The excellent fracture resistance of such disordered GBs is most commonly attributed to their large GB excess free volume, which enhances the atomic shuffling events during GB-dislocation interactions and thus mitigates damage. However, it has been found that the introduction of non-equilibrium GBs with large excess free volume in elemental tungsten cannot suppress the intergranular fracture [39]. This suggests that the GB excess free volume alone, which is sensitive to the GB topological features, may not be the only factor determining the GB fracture resistance. Indeed, the aforementioned disordered GB structures are often obtained by element segregation, where the topological disorder and chemical disorder are coupled together. It is thus of interest to explore the role of inhomogeneous chemistry distribution on the GB deformation and fracture, since GB can be concentrated in multi-principal solution with disordered chemistry even if in a dilute multicomponent alloy [40]. Given the tendency that changing the GB chemistry becomes one of the key strategies for tailoring GB properties, it would be meaningful if we could specify how the GB chemistry affects the GB fracture response.

The recently emerging high/medium entropy alloys (H/MEAs) or called complex concentration alloys (CCAs) can serve as good model systems for studying such issues, because their intrinsic chemical inhomogeneity is beneficial to decouple the entangled topological and chemical disorder. It was found that CoCrNiFeMn HEA and its derivations exhibit a rapid decrease in ductility by intergranular fracture at intermediate temperatures due to the nanoclustering of multi-principal elements in GB [41,42]. Yang et al. discovered that nanoscale chemical disordered GB layer driven by multi-element co-segregation can effectively prevent brittle intergranular fractures by enhancing dislocation motilities in a NiCo-based HEA with ordered superlattice structure [43]. These results seem to highlight the role of chemical inhomogeneity in inhibiting GB fracture. It still needs to clarify how the chemical inhomogeneity controls the GB atomic shuffling and fracture mode. Such information is important for the design of suitable GB chemistry for enhancing GB strength and toughness in the infinite composition space of HEAs.

Precise characterization of atomic motion and cracking events within GB by experimental observations is an extremely difficult enterprise, especially for the HEAs that exhibit severe structure distortion and chemical fluctuations [17,44-46]. Atomistic computer simulations, in this respect, allow one to focus on the atomic deformation evolutions and interactions, and have proven to be an invaluable tool for the study of GB behaviors [6,7,18,33,34,47-51]. We therefore resort to MD simulations combined with first-principles DFT calculations here, to elucidate the atomic and electronic level origin and pathway of GB deformation and fracture. For simplicity, we take the ternary NiCoCr medium entropy alloy, which exhibits an excellent combination of mechanical properties including high strength, large ductility, and high fracture toughness at ambient-to-cryogenic temperatures [52–55], as a model system to minimize the complex element interactions while retaining its disordered chemistry.

2. Methods

2.1. Molecular dynamic GB tension simulation

Several symmetrical tilt GBs including $\Sigma17(140)[001]$, $\Sigma29(730)[001]$ and $\Sigma5(210)[001]$, which have the same [001] tilt axis, but different tilt angles, were chosen as model systems representing typical high-angle GB and different spatial arrangements of polyhedral packing units. The bi-crystal models contain two identical symmetrical tilt GBs separated by a sufficient thickness of ~18 nm, as shown in Fig. 1(a). A wire geometry is used here to allow for shear offsetting and necking. The cylindrical wire samples containing ~1000,000 atoms with a diameter of 19 nm and height of 36 nm were cut from the initial bi-crystal blocks, as illustrated in Fig. 1(a). To create chemically disordered GB chemistry, the lattice is randomly occupied by Ni, Co and Cr with equal molar ratios (see Fig. 1(b)). The bi-crystal samples are remodeled to pseudo-element models by adopting the derived hypothetical pure average-atom interatomic potential which bears the same bulk properties of equiatomic CrCoNi HEA but no chemical fluctuation [56,57], to eliminate the effect of chemical inhomogeneity (see Fig. 1(c)). For $\Sigma5(210)[001]$ GB, three different GB atomic topological structures are considered, which are obtained by GB structural transition via isothermal annealing at different temperatures, as detailed in Ref. [45]. They include orderly "Kite" structure units (labeled R-K/A-K GB), partially ordered "Filled Kite" (R-FK/A-FK GB) and disordered "pre-melting" (R-PM/A-PM GB) structures (see Fig. 2).

MD simulations were performed using the Large-scale Atomic/Molecular Massively Parallel Simulator (LAMMPS) package [58] with a DFT-calibrated embedded-atom potential for CrCoNi HEAs by Li et al. [59]. Periodic boundary conditions were applied in the y direction, and the free-boundary condition was applied in the x and z direction. The models were deformed under tensile loading by applying a constant strain rate of 10^8 s^{-1} perpendicular to the GB plane (y direction) by using the NVT ensemble equations of motion for a temperature of 10 K, at which thermal perturbations and GB diffusion are somewhat suppressed. The visualization of the atomic configurations was performed using the Polyhedral Template Matching (PTM) method [60] implemented in the OVITO software [61].

2.2. Molecular statics mode-I crack propagation simulation

We also examine the explicit simulation of crack-tip processes by using a mode-I crack propagation simulation based on molecular statics, taking various $\Sigma5$ (210) GBs as examples. Cylindrical bi-crystal configuration with a radius of 19 nm and thickness of 18 nm containing a $\Sigma5$ (210) GB along the central plane is adopted here, as shown in Fig. 1(d). Before the loading process, an atomically sharp crack is introduced at the center by displacing the atoms according to the linear-elastic (LEFM) solution for the near field displacements around a crack tip under plane-strain conditions [62]:

$$u_x = \frac{K_I}{G}\sqrt{\frac{r}{2\pi}}\cos\left(\frac{\theta}{2}\right)\left[1-2\nu+\sin^2\left(\frac{\theta}{2}\right)\right] \quad (1)$$

$$u_y = \frac{K_I}{G}\sqrt{\frac{r}{2\pi}}\sin\left(\frac{\theta}{2}\right)\left[1-2\nu+\cos^2\left(\frac{\theta}{2}\right)\right] \quad (2)$$

where K_I is the mode-I stress intensity factor, r and θ are the cylindrical coordinates with the crack tip position. G is the shear modulus and ν is the Poisson's ratio, both of which values are very close in CrCoNi potential and average-atom potential, as shown in Table 1.

The crack is loaded by assigning an incremental displacement field according to the mentioned LEFM equation, which corresponds to an increment of stress intensity factor by $\Delta K_I = 0.01$ MPa $m^{1/2}$, based on the position of a new crack tip, step by step. After that, the crack configuration is relaxed with the FIRE algorithm with a convergence criterion of 10^{-8} eV/Å, when the atoms in the boundary layer (with a thickness of 10 Å) were kept fixed in order to prescribe the predefined stress intensity

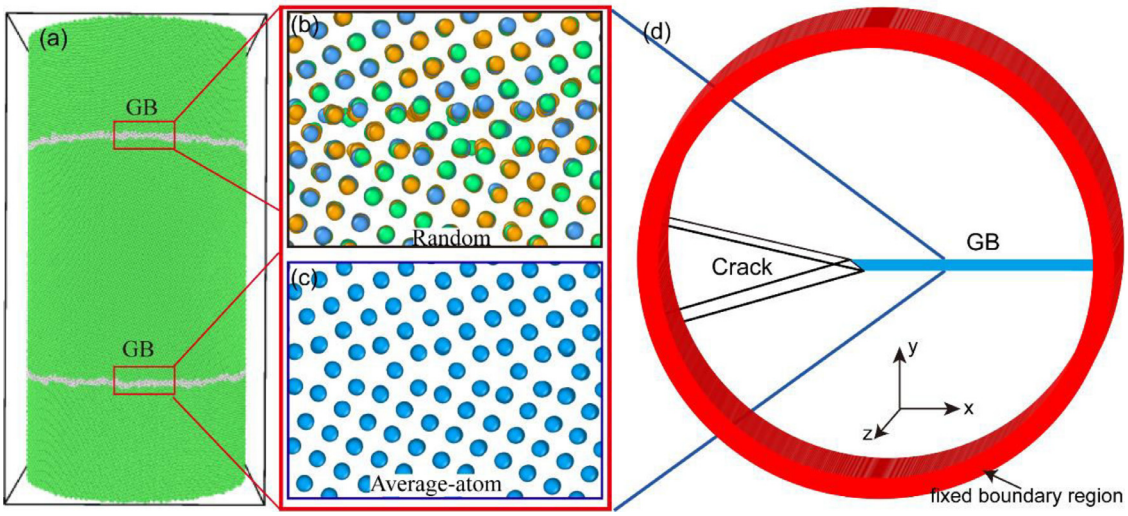

Fig. 1. (a) Bi-crystal wire model containing two identical GBs. The surface atoms are removed to exhibit GB position: (b) representative GB structure with random chemical distribution, (c) representative GB structure with average atom potential. The blue, yellow and green spheres denote Co, Cr and Ni, respectively. (d) Schematic illustration of the setup for simulations of mode I grain boundary cracks.

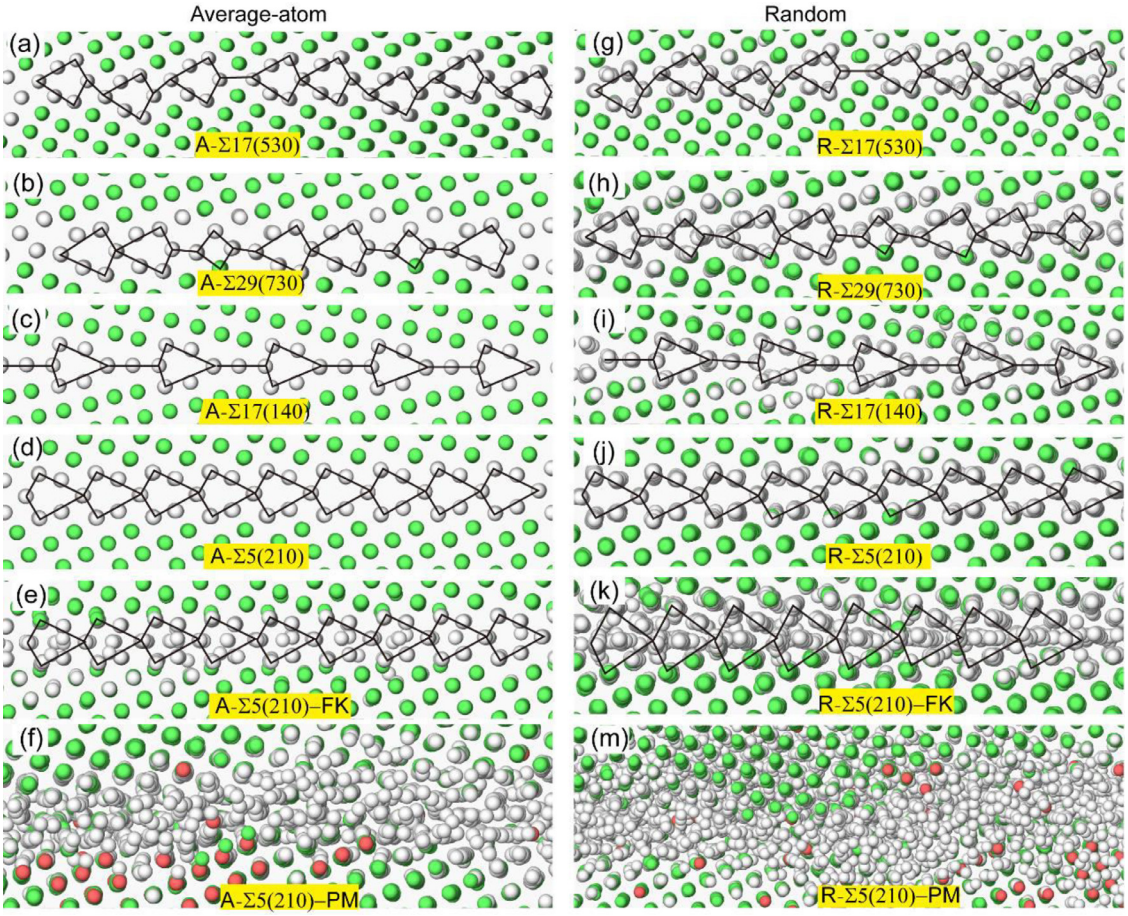

Fig. 2. Magnification of the GB structures for (a–e) average-atom GBs and (f–m) chemical disordered GBs after relaxation. Established repeating structural units are indicated by black lines.

Table 1
Bulk modulus (B), Shear modulus (G), Poisson's ratio (ν), intrinsic (γ_{isf}) and unstable (γ_{usf}) stacking fault energy calculated by CrCoNi potential and average-atom potential.

Sample	B (GPa)	G (GPa)	ν	γ_{isf} (mJ/m^2) [56]	γ_{usf} (mJ/m^2) [56]
Random	203.3	71.84	0.355	−14.97	310.34
average-atom	208.3	77.46	0.346	−25.46	321.34

while the atoms belonging the inner region are allowed free evolution under the constraints of the boundary region. Periodic boundary conditions are used along the cylinder axis, which corresponds to the crack front direction and the GB tilt axis ([001] direction).

2.3. First-principles calculations

To further study the physical mechanisms of GB atomic deformation, DFT calculations were carried out using a plane wave method, as implemented in the Vienna Ab initio Simulation Package (VASP) [63]. A category of quasi random (210) surface supercells containing 120 atoms was generated through a Monte Carlo (MC) algorithm using the Alloy Theoretic Automated Toolkit (ATAT) package developed by Alex van de Walle et al. [64]. These random (210) surface supercells were then transformed symmetrically to create the sandwich Σ5 (210) STGB supercells with Kites GB configuration.

The quasi-static tensile simulations are conducted using a method described previously by Roundy et al. [65]. The lattice vectors of the supercells are deformed incrementally in the direction orthogonal to the GB plane. At each deformation step, the structure and atoms are relaxed such that all the average residual components of the Hellmann-Feynman stress tensor orthogonal to the applied strain and the average force on each atom are below 0.1 GPa and 0.01 eV/Å, respectively, while keeping the applied strain fixed. A gradient-corrected functional in the Perdew-Burke-Ernzerhof (PBE) form was used to describe the exchange and correlation interactions in DFT [66]. Electron-ion interactions were treated within the projector-augmented-wave (PAW) method [67]. A sufficiently high energy cutoff of 380 eV was adopted for the plane-wave basis set expansion. Brillouin zone integrations were performed using $3 \times 3 \times 1$ Monkhorst-Pack k-point grids. In the energy minimization process, structures were optimized until the atomic forces become less than 0.01 eV/Å. Collinear spin polarization (ISPIN = 2) is enabled in all the calculations.

3. Results and discussion

3.1. Effect of chemical inhomogeneity on GB structure

We begin by investigating the relaxed GB atomic structures with random chemical distribution and pseudo-elemental chemistry, where the total atomic number is equal. A magnified view of the various GB structures is shown in Fig. 2. For the equilibrium GBs with different misorientations, all the pseudo-elemental GBs exhibit a regular GB structure with continuously repeating structural units (SUs) (Fig. 2(a–c)), as marked by black lines. The chemical disordered GBs (Fig. 2(f–h)) show these repeating units as well, despite the interior angles of such kite shapes structural units being slightly different. This suggests that the disordered chemical distribution cannot drastically alter the equilibrium GB structure. Similar result was also found in the Σ11(332)[110] STGB for CuNiCoFe HEA [68]. By comparing the structure for a series of random [110] tilt GBs, Farkas [69] demonstrated that the chemical disordered GBs exhibit less local non-planar structures and average dislocation content than the corresponding "average atom" GBs. We failed to observe similar results since the dislocations are in oblique planes in the [100] tile GBs studied here, which are difficult to form only by structural relaxation. Even so, apparent structural distortions are found in the chemical disordered GBs, resulting in extra unidentified atoms and even affecting the GB width. Such distortion can be contributed to the apparent difference in interatomic bond length between different atom pairs [45].

Fig. 2(c–e) and (h–k) shows the atomic structure of Σ5(210) GBs with various topological structures and chemical distributions. In comparison, the effect of chemical disorder on GB structure is more pronounced with increasing topological disorder. As mentioned, the introduction of chemical disorder on the ordered A-K GB leads to only moderate structural distortions without fundamental structural changes. Despite the shape of the structural units being overall similar for A-FK and R-FK GB, the atomic packing within the structural units is severely distorted and more disordered for R-FK GB, presenting a semi-disordered topological distribution (see Fig. 2(d) and (i)). For the topological disordered PM GBs, the chemical randomness leads to a higher width and atomic density, as shown in Fig. 2(e) and (k). These suggest that chemical disorder aggravates structural disorder. Even so, the topological disorder for these GBs is roughly with the order of A-*K*<*R*-*K*<A-FK<*R*-FK<*A*-PM<*R*-PM, suggesting that chemical disorder does not change the topological state fundamentally.

3.2. Overall damage evolution

Fig. 3 shows the tensile stress-strain behavior of the various considered GB configurations. Interestingly, the overall trend of stress-strain response can be classified by GB chemistry rather than GB type and GB atomic topological distribution. After the initial stress drop, the pseudo-element bi-crystals exhibit a significant strain softening behavior, manifested as a continuous decrease of flow stress with strain as shown in Fig. 3(a) and (c). In contrast, for chemical disordered bi-crystals, a stress plateau is observed after initial stress drops, resulting in a higher failure strain, see Fig. 3(b) and (d). This stress plateau corresponds to a stable plastic flow process. The distinct stress-strain response indicates a different deformation or failure mode between pseudo-elemental and chemical disordered GBs. The observation on the deformation snapshots near the failure stage reveals that all the considered pseudo-elemental GBs are fractured by cracking, including the various GBs with different misorientations (see Fig. 3(a)), and the same GB with different topological structures where the thickness, atomic arrangement and atomic density are quite different (see Fig. 3(b)). This suggests that under this pseudo-elementary GB chemistry, the GB fracture properties cannot be fundamentally changed by altering atomic topological distribution alone, even if topological disordered structures are formed. A similar result was found in elemental tungsten, where disordered GBs with large excess free volume failed to suppress intergranular fracture [39]. In contrast, the fracture mode can change abruptly by introducing chemical inhomogeneous, as demonstrated by the distinct fracture behavior between A-K and R-K GBs that exhibit the same ordered GB atomic stacking but different GB chemical distributions. Indeed, all the chemical disordered GBs are uncracked even if the corresponding bi-crystals are fractured by intragranular necking at large strain. These results highlight the decisive role of chemical heterogeneity in inhibiting GB fracture.

For simplicity, in the following analysis, we focus on the six Σ5(210) GBs with different chemical distributions and topological structures. Fig. 4 shows the detailed structural evolution of A-PM GB and R-PM GB, which represent the pseudo-elementary and chemical disordered GB respectively. In the early stage of plastic deformation, these two classes of GBs exhibit similar evolution processes. In both GBs, dislocations are initiated from the interior of the GB rather than from the free surface, suggesting that the incipient plastic behavior is not affected by the presence of high energy surfaces within the circular nanowire geometries. As the strain increases, more dislocations emanate from GBs and propagate inside until annihilation at free surfaces. After that, a crack is nucleated at the intersection of free surface with A-PM GB, which propagates continuously along GB and causes fracture eventually (see the last two frames in Fig. 4(a)). Conversely, the R-PM GB is deformed homogeneously without any obvious cracks or voids, and necking instability occurs at the interior of grain finally (see

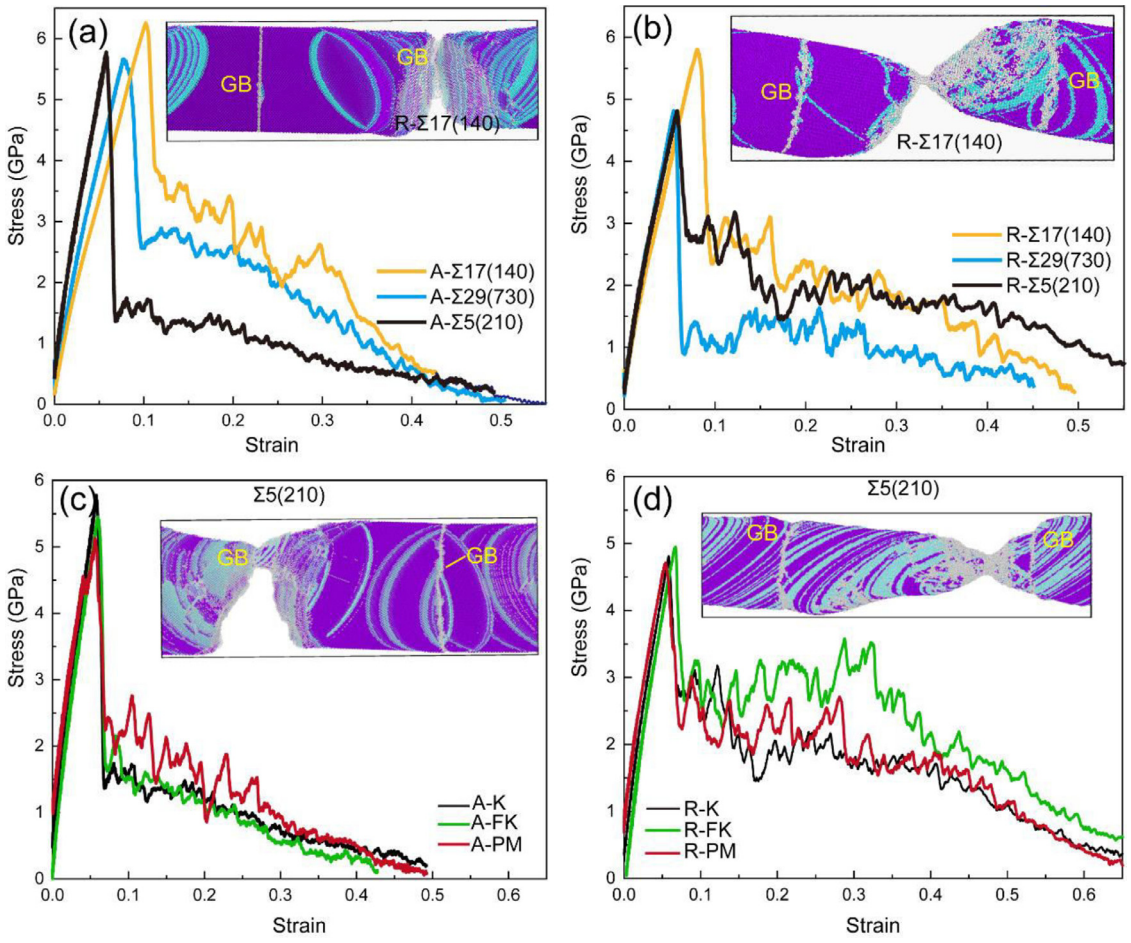

Fig. 3. Tension stress-strain responses of various GB configurations. (a) Pseudo-element GBs and (b) chemical disordered GBs with different GB types; (c) Pseudo-element GBs and (d) chemical disordered GBs with the same GB type but different atomic topological structures obtained by annealing of Σ5(210) GB. The deformation snapshots near the failure stage are provided inset, in which the FCC, HCP and amorphous structures are colored in purple, cyan and gray, respectively. The surface atoms (with a thickness of 5 Å) are deleted for easy observation.

Fig. 4(b)), suggesting a strong GB deformability for these chemical disordered GBs. The statistical results of dislocation number near GB show that there is no significant difference in dislocation density between A-series and R-series models, which can also be inferred from their approximate stacking fault energy shown in Table 1. Therefore, the different fracture behavior between R-series and A-series GBs is caused by the chemical disorder.

In order to give a more quantitative sense of the toughening effect of disordered GB chemistry, we have traced the damage evolution for all the considered Σ5(210) GBs. A surface atom technique based on the distribution of Voronoi volumes is adopted to quantify the GB damage evolution, since the formation of cracks or voids leads to an increase in atomic Voronoi volume. A threshold Voronoi volume of 17 $Å^3$, larger than the average value of 10–15 $Å^3$ in equilibrium, was used to identify the GB-damaged atoms. Fig. 5(a) shows the number of void atoms as a function of strain for each GB. A significant increase in the number of voids is found in the pseudo-element GBs after ~7% strain, at which point abundant dislocations have formed in the GBs (see Fig. 4). This suggests that the nucleation of cracks is related to the GB-dislocation interaction at the early deformation stage. Inversely, only a small fraction of voids are identified in the chemical disordered GBs after large deformation, which are associated with necking-induced surface damage.

The formation of GB voids and cracks usually has been attributed to the strain/stress localization caused by GB-dislocation interaction [70,71]. It has also been suggested that the high stress triaxiality η, which is defined as the ratio of the hydrostatic stress to the von Misses effective stress, is the driving force for the formation and growth of void and crack [37,72-75]. A large η denotes a hydrostatic stress domination state, which is apt to void and crack growth. Otherwise, shear deformation dominates for a small η value. As demonstrated in Fig. 5(b), a concentrated high η region is observed within A-PM GB region, which could produce a void immediately with a very small increment in the applied strain (6.9% to 7.0%). This suggests that stress triaxiality η can be used to characterize the damage-related atomic property.

We calculated the average stress triaxiality η in both the pseudo-element and chemical disordered GBs as a function of applied strain, and the results are shown in Fig. 6(a) and (b) respectively. Overall, the peak stress triaxiality η in pseudo-element GBs is much higher than chemical disordered GBs, corresponding to the aforementioned results that pseudo-element GBs are more apt to crack. A closer comparison reveals that both the initial and the incremental η values in pseudo-element GBs are much higher than that of corresponding chemical disordered GBs. Fig. 6(c, d) shows the spatial distribution of stress triaxiality η at various strain states for A-PM and R-PM GBs. Initially, the η in GBs is higher than intragranular, indicating that GBs are more vulnerable to damage nucleation. As the GB dislocation increases, the concentrated high stress triaxiality is alleviated in some GB regions due to atomic shear deformation. Even so, the remainder high η region in A-PM GB still

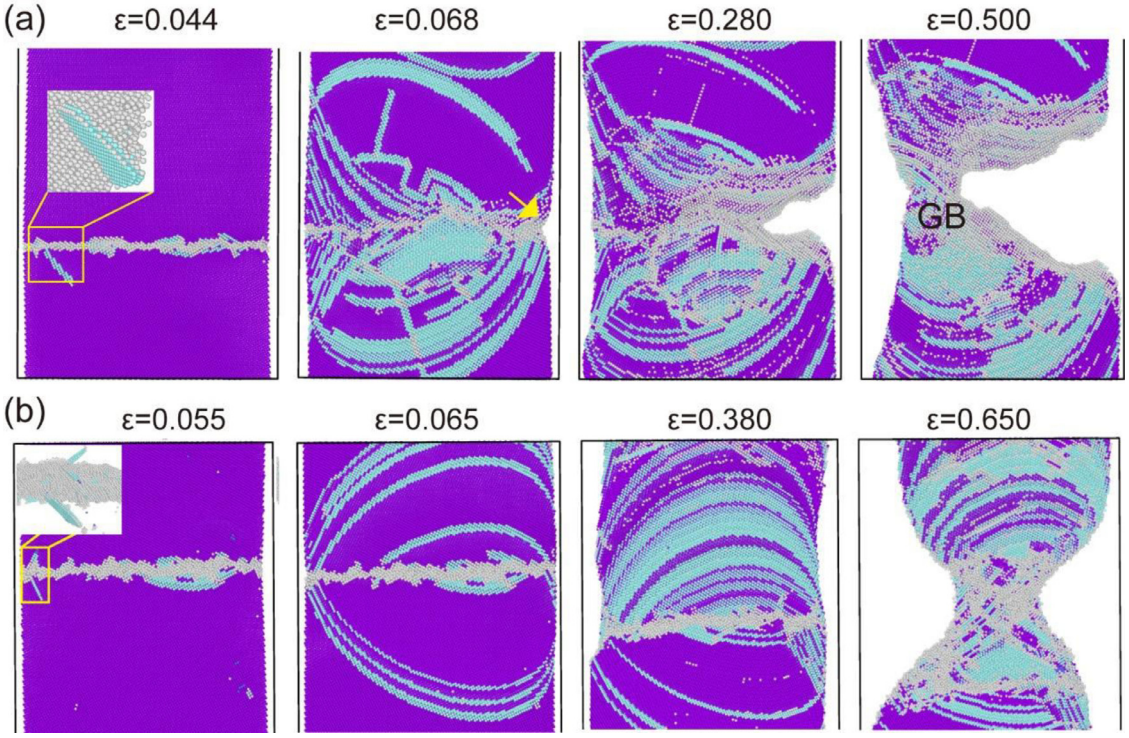

Fig. 4. Snapshots of (a) A-PM and (b) R-PM bicrystal with Σ5(210) GB at different deformation stages. Images are colored according to the CNA parameter. Atoms colored purple are the FCC atoms; cyan represents the HCP atoms; structures other than FCC and HCP are colored gray. The surface atoms (with a thickness of 5 Å) are deleted for easy observation.

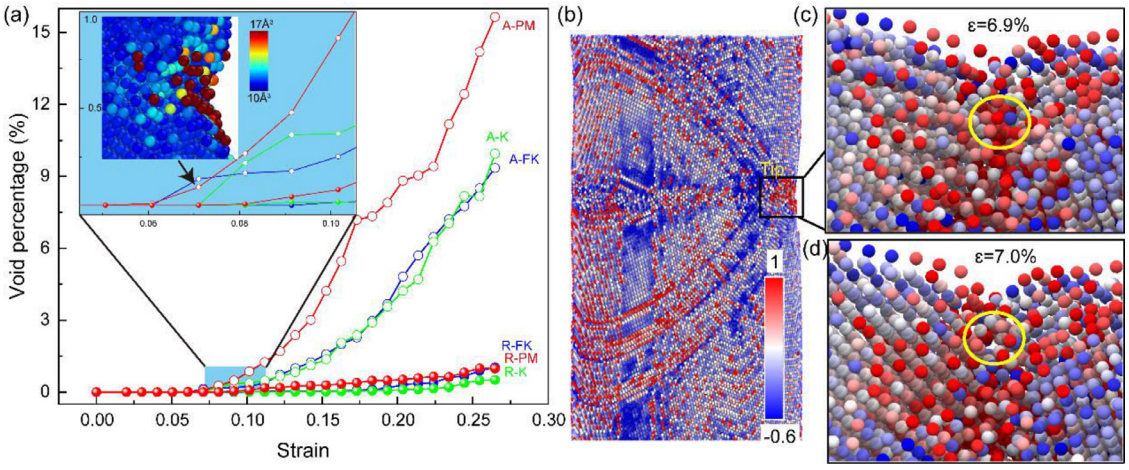

Fig. 5. Formation and evolution of voids in GBs: (a) void volume fraction for all considered GBs as a function of strain, along with the distribution of void atoms in A-PM GB at ε =7.0%, (b) the distribution of stress triaxiality η in the A-PM bicrystal at the strain of 6.9%, (c) a larger version of high η region in Fig. 5(b) (indicated by the black box), (d) the high η region at a slightly higher strain ε = 7.0%.

promotes the nucleation of voids, which, in turn, leads to a high η region ahead of the crack tip, as shown in Fig. 6(c). As such, voids constantly form ahead of crack tip with high η, driving crack propagation. While for chemical disordered GBs the peak η value is relatively lower, suggesting a shear dominate atomic deformation that prevents void or crack formation. As shown in Fig. 6(d), although the η in GB is also slightly higher than the interior, there is no obvious high η concentrated region in the representative R-PM GB. Based on the above analysis, the high stress triaxiality accumulated during the early deformation is responsible for the nucleation of voids in these pseudo-element GBs.

3.3. GB crack propagation

In order to exclude the possible highly over-driven situation for crack propagation during high strain rate MD loading, we performed a mode-I crack propagation simulation based on molecular statics by using a K-test methodology [34,76,77]. Fig. 7 plots the GB crack propagation distance as a function of applied stress intensity factor. As shown, the crack propagation distances in the chemical disordered GBs are far less than pseudo-elemental GBs, regardless of atomic topological distribution and crack direction. This clearly demonstrates the strong fracture resistance of chem-

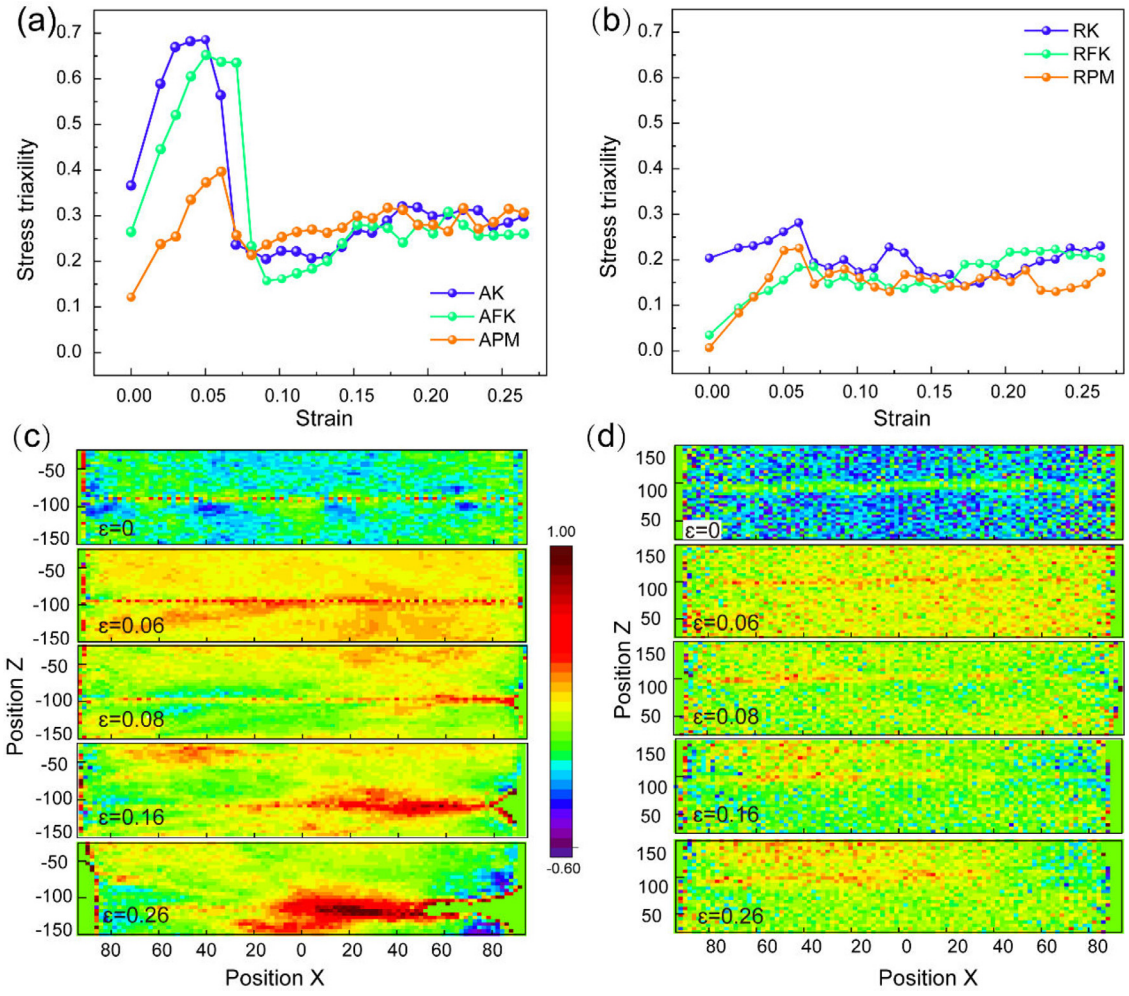

Fig. 6. Evolution and spatial distribution of stress triaxiality η in both the pseudo-element and chemical disordered GBs. (a) η in pseudo-element GBs as a function of strain, (b) η in chemical disordered GBs as a function of strain, (c) spatial distribution of η in A-PM GB at various strain states, (d) spatial distribution of η in R-PM GB at various strain states.

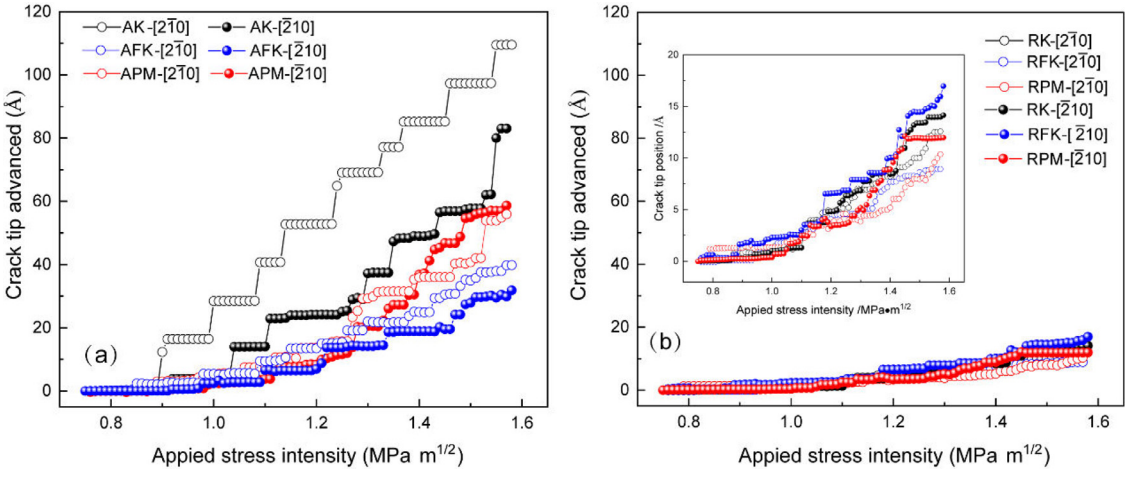

Fig. 7. (a) Pseudo-elemental and (b) chemical disordered GB crack advances as a function of applied stress intensity along [$\bar{2}$ 1 0] and [2 $\bar{1}$ 0] directions.

ical disordered GBs, which is in qualitative agreement with the results observed in direct GB tension simulations. To understand this trend in theory, we calculated the critical stress intensity factor (K_{IG}) according to the Griffith theory for all considered GBs and the results are listed in Table 2. As shown, the theoretical cleavage stress intensity factor is more sensitive to GB topology than chemistry, in which the K_{IG} between counterpart pseudo-element

Table 2
Theoretical cleavage stress intensities for all grain boundaries studied here.

GB	K_{IG} (MPa m$^{1/2}$)	GB	K_{IG} (MPa m$^{1/2}$)
A-K	0.89	R-K	0.82
A-FK	0.65	R-FK	0.69
A-PM	0.47	R-PM	0.52

and chemical disordered GBs is very close and it decreases significantly with the increase of disorder with the order of *K*>FK>PM in both. Indeed, the Griffith criterion for crack propagation in terms of continuum properties neglects the underlying atomic nature and the complex low-energy surface topography that changes the local crack tip stress intensity. At atomic scale, crack-propagation resistance should be characterized by the force required to break the bonds directly at the crack tip region rather than a global energetic criterion [18,25,34]. The complex discrete atomic arrangement within GB provides many high toughness regions that can arrest the crack tip and thus require a higher stress intensity factor for crack growth, as so-called bonding trapping effect. In this light, the discrepancy between theoretical predictions and simulation results actually reflects the complex interactions of GB atoms, which would be more pronounced in the chemical disordered GBs.

Fig. 7 also shows a significant difference in the trend of crack growth curves between pseudo-elemental and chemical disordered GB, suggesting a different crack propagation path between them. For pseudo-elemental GBs, the crack propagation distance increases stair-stepping with increasing stress intensity. This trend is somewhat disturbed in topological disordered APM GB, which further weakened in chemical disordered GBs. Furthermore, crack propagation in pseudo-elemental GBs exhibits an apparent directional anisotropy and topological dependence, as manifested by the apparent difference in crack growth rate for different directions and GB topologies in Fig. 7(a). While for chemical disordered GBs, the crack growth rate is independent of atomic topology and crack direction, as shown in the inset of Fig. 7(b). All of these suggest that the chemical distribution characteristic of GB atoms is a crucial factor in GB fracture for such HEAs, overwhelming the crack direction and the GB topology.

The stair stepping of crack advance in A-K and A-FK GBs can be attributed to the periodicity of the structural unit, in which the bond-breaking energy is different in different sites within these structural units [25]. Usually, the directional anisotropy of a crack can be explained by means of Rice theory which defined a critical stress intensity factor for dislocation nucleation on a slip system available at the crack tip, which depends on the relative orientation between the slip system and crack system [78]. However, there are no slip planes containing the crack front in current Σ5(210)GB so that any emission is on oblique planes, which is outside the scope of the Rice theory [18]. Therefore, the directional anisotropy of GB crack propagation can be understood in terms of the bond trapping effects. But this does not imply the absence of bond trapping effects in topology disordered APM GB and all chemical disordered GBs, although the periodicity and the directionality of crack propagation are diminished or even disappeared. Instead, it can be understood by considering the random distribution of high energy trapping sites in these disordered GBs.

Figs. 8 and 9 show the key atomistic configurations during crack propagating along [2 $\bar{1}$ 0] direction of pseudo-elemental and chemical disordered GBs, respectively. As shown in Fig. 8(a1), ordered A-K GB begins to cleave at 0.92 MPa $m^{1/2}$, which is close to the theoretical value predicted by Griffith theory. After that, the crack propagates discontinuously with increasing stress intensity factor. For A-FK GB, the critical stress intensity for crack propagation is 0.97 MPa $m^{1/2}$, 50% higher than the theoretical value shown in Table 2. After that, a local atomic rearrangement occurs at crack tip, which hinders the crack from propagating until the load has been increased to 1.15 MPa $m^{1/2}$. This rearrangement process is repeated for loading and results in a gentle stepwise advance of crack tip. Similar processes are found in the A-PM GB, in which crack begins to advance at a high load of 1.12 MPa $m^{1/2}$ that more than twice the predicted theoretical value. The large stress intensity factor for crack propagation in A-FK and A-PM GB suggests strong lattice trapping effects and fracture resistance in them. It should be noted that for these pseudo-element GBs in both directions, there is no dislocation emission from the crack tip until the complete fracture. This may relate to the fact that there are no slip planes containing the crack front in current Σ5(210) GB that any emission is on oblique planes, which requires high loads exceeding the fracture thresholds for them. Therefore, the trapping effect exhibited in the A-FK and A-PM GBs may arise from the local atomic rearrangement at crack tip, which leads to local plasticity via atomic shear.

Fig. 9 shows the crack evolution in chemical disordered GBs with increasing stress intensity. As shown, the cracks in all the chemical disordered GBs advance very slowly even under a high stress intensity. Examining the atomistic configurations reveals that the crack tips undergo substantial reconstruction and form a local amorphous region with increasing loads. Similar amorphization at the crack tip was also observed in CrMnFeCoNi HEA by MD simulations [79] and experiment [80]. It should be noted that partial dislocations can be observed ahead of the crack tip at a higher load of ~1.4 MPa $m^{1/2}$ in R-K and R-FK GBs along [$\bar{2}$ 1 0] direction. Even though, the obvious tip reconstruction is the main reason for preventing crack propagation, since the emission of dislocation results from the combination effect of high stress state and rearrangement of crack tip atoms. Such tip reconstructions not only change the crack tip geometry and topology, i.e. blunting and amorphization, but also diminish the stress concentration around crack tips through a complicated “plastic” process. In turn, these amorphous crack tip regions can trigger atomic plastic deformation through the ongoing operation of the shear transformation zones during loading. This may be responsible for the absence of dislocation in the crack tip for highly amorphous R-PM GBs. All of these reduce the driving force for crack propagation and thus prevent it effectively. By comparison, the atomic rearrangements at crack tips for pseudo-elemental GBs are very limited even if in the topological disordered A-PM GB. This suggests that the GB chemical heterogeneity effectively facilitates structural rearrangement at crack tip and hence prevents crack propagation.

Recall that high stress triaxility is an important driving force for crack nucleation and growth. The distinct crack propagation behavior of pseudo-elemental GBs and chemical disordered GBs can also be explained by their different stress states of crack tip atoms. Take the R-K GB under stress intensity factor of 1.00 MPa $m^{1/2}$ as an example, we plotted the stress triaxiality distribution along GB in Fig. 10(a). An obvious stress peak appears at the crack tip, in good agreement with the results observed in GB tensile simulations shown in Fig. 6. Fig. 10(b) shows the evolution of the maximum of stress triaxiality in crack tips for all considered Σ5(210) GBs. Interestingly, the stress triaxiality undulates periodically with increasing stress intensity factor, in which the drop points roughly correspond to the crack advance processes. All of these highlight the dominant role of high stress triaxiality on crack propagation. In current K-test simulations, a larger normal tensile stress component is required to endow Model I fracture [81], resulting in a respective high tip stress triaxiality. Nonetheless, the tip stress triaxiality in chemical disordered GBs is still much lower than that in pseudo-elemental GBs, again in agreement with the MD tension results, indicating a much lower driving force for crack propagation and thus much slower crack growth rate for the chemical disordered GBs.

3.4. Atomic mechanism for preventing GB fracture

Note that the considered NiCoCr MEA models are obtained by random occupying of different elements without any intended segregations. Even so, these random NiCoCr GB models show opposite fracture behaviors of the pseudo-elementary GBs. This highlights the positive effect of disordered chemical distribution on fracture

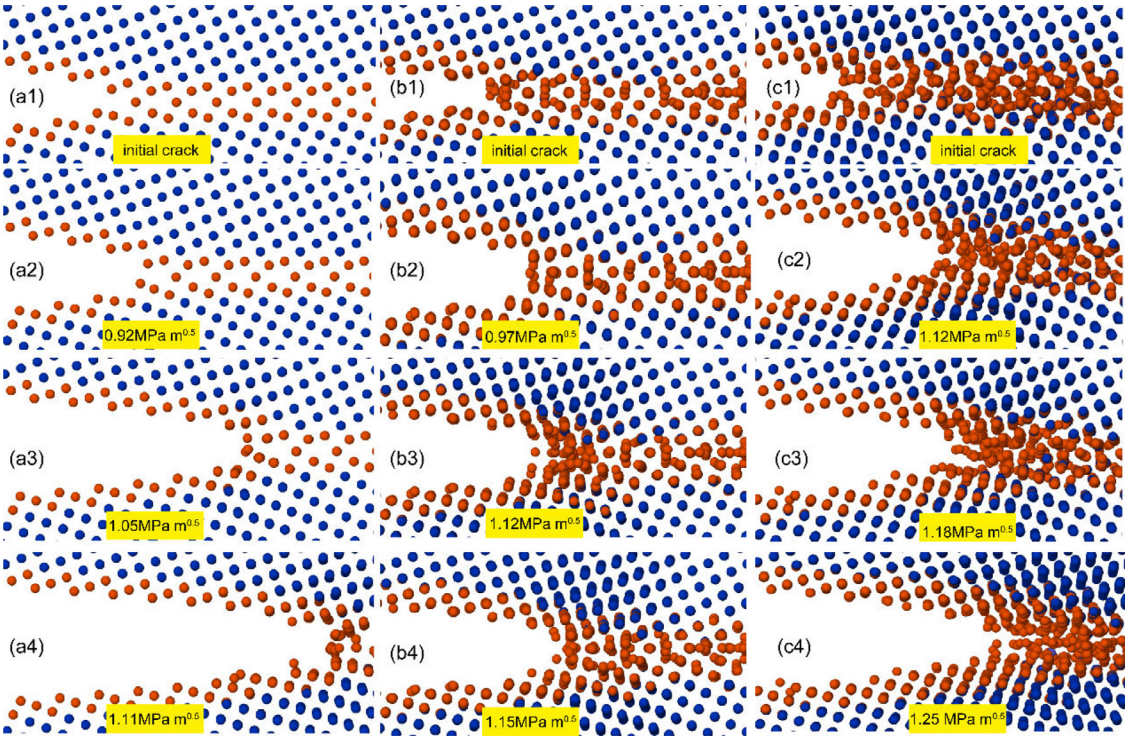

Fig. 8. Process of an intergranular crack propagation in A-K (a1–a4), A-FK (b1–b4) and A-PM (c1–c4) GBs along [2 $\bar{1}$ 0] direction. Atoms colored by Common Neighbor Analysis (Blue: FCC; Orange: others).

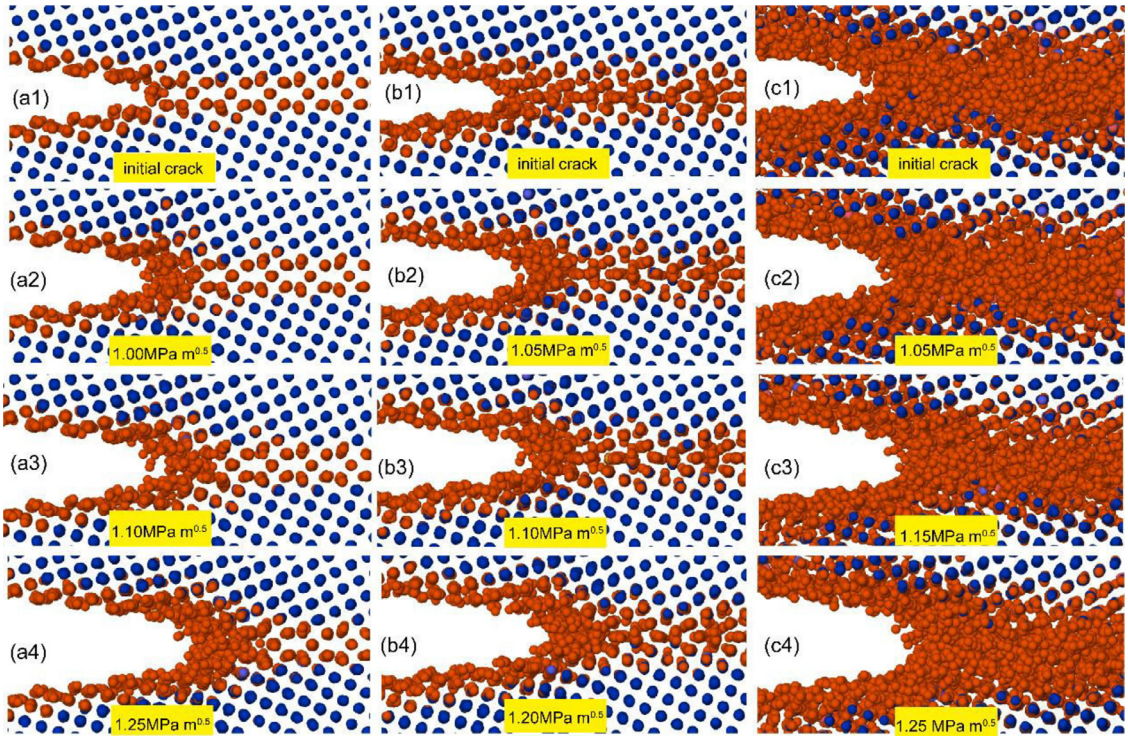

Fig. 9. Process of an intergranular crack propagation in R-K (a1–a4), R-FK (b1–b4) and R-PM (c1–c4) GBs along [2 $\bar{1}$ 0] direction. Atoms colored by Common Neighbor Analysis (Blue: FCC; Orange: others; Green: HCP).

resistance. To understand the atomic origin of the chemical disorder controlled GB toughening, a comprehensive analysis of the GB atomic kinematics such as slip vector [82], dilatation and shear factors [83] is performed based on the GB tensile results. Fig. 11(a) shows the dependence of average GB atom slip vector on the applied strain, in which the surface atoms (with a thickness of 5 Å) are deleted to eliminate surface effects. The atomic slip vector defines the relative displacement between atoms and their surroundings, and can be calculated by $S^{\alpha} = -\frac{1}{n_s}\sum_{\beta\neq\alpha}^{n}(x^{\alpha\beta} - X^{\alpha\beta})$, where n is the number of nearest neighbors of atom α and n_s is the num-

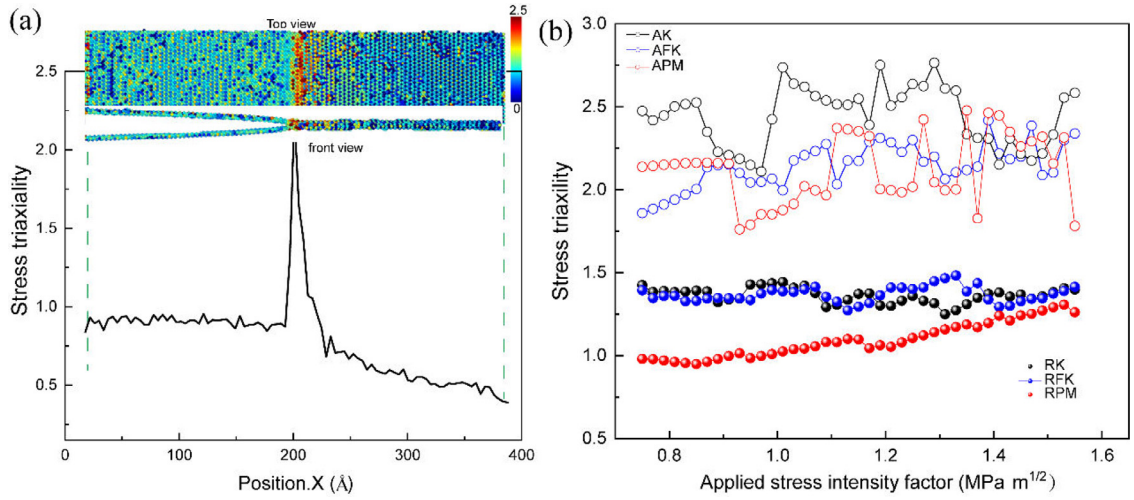

Fig. 10. Distribution and evolution of stress triaxiality among all considered GBs. (a) Distribution of stress triaxiality within GB as an example of RK GB under stress intensity factor of 1.00 MPa $m^{1/2}$. (b) Evolution of the maximum of stress triaxiality in crack among all considered GBs.

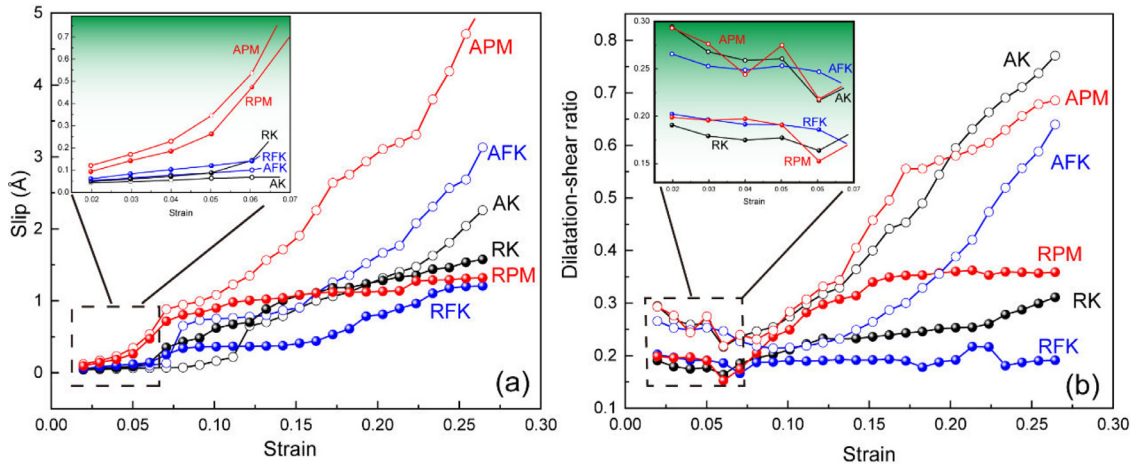

Fig. 11. (a) Variation of average atomic slip vector versus applied strain, the inset shows magnified regions before void nucleation. (b) Dilatation-shear ratio as a function of strain.

ber of slipped nearest neighbors, superscript $\alpha\beta$ denotes the interatomic vectors of atom α and β, and $x^{\alpha\beta}$-$X^{\alpha\beta}$ represent the vector differences of $\alpha\beta$ between deformed and reference configurations. As shown in Fig. 11(a), the atomic slip vector in all the Σ5(210) GBs increases slowly with strain in early stage, followed by a rapid increase due to dislocation emission. Thereafter, the slip vectors in the pseudo-element GBs increase continuously due to GB crack formation and propagation, while it tends to be constant for chemical disordered GBs. As shown in the inset of Fig. 11(a), the slip vectors in the GBs with similar topology are comparable at the initial deformation stage that controls the stress triaxiality accumulation and thus damage nucleation, in which the slip vectors in topological full disordered GBs (A-PM and R-PM) are higher than others. This suggests that the atoms in topology disordered GBs possess a higher mobility and promote GB atomic shuffling.

The minor difference in the slip vector between A-series and R-series GBs at the damage incubation stage suggests that the atomic displacement behavior alone is insufficient to explain the large difference in the fracture behavior between pseudo-element and chemical disordered GBs. Actually, the deformation of GB atoms is intertwined by atomic shear and dilatation or contraction, where the atomic shear reflects the degree of plastic deformation while atomic dilatation contributes to crack/void formation [73,84]. To characterize the relative degree of atomic shear deformation and dilatation, we calculate the ratio of dilatation factor to shear factor (named dilatation-shear ratio), which are calculated by introducing the scalar products of decoupling shear and dilatation deformation tensors [83]. This dilatation-shear ratio can also qualitatively reflect the stress triaxiality, since both reflect the competition between atomic shear and expansion.

Unlike the slip vector, the atomic dilatation-shear ratio depends on the GB chemistry rather than the GB topology, as indicated by the distinct fracture modes between A-series and R-series GBs. At the damage incubation stage, the dilatation-shear ratios in pseudo-element GBs are significantly higher than that in chemical disordered GB, regardless of the GB topology, as marked by the dotted box and enlarged in the inset of Fig. 11(b). After that, the dilatation-shear ratio in pseudo-element GBs increases continuously and rapidly, which is associated with the continuous void formation and crack propagation. However, for chemical disordered GBs, the dilatation-shear ratio fluctuates around a constant value after a slow increase, which corresponds to stable GB plastic deformation without significant damage. The low dilatation-shear ratio for such chemical disordered GBs suggests a shear-dominated atomic deformation, as evidenced by the drastic atomic rearrangement at the crack tips during static fracture simulations. This also corresponds to the low stress triaxiality and high fracture resistance for chemical disordered GBs.

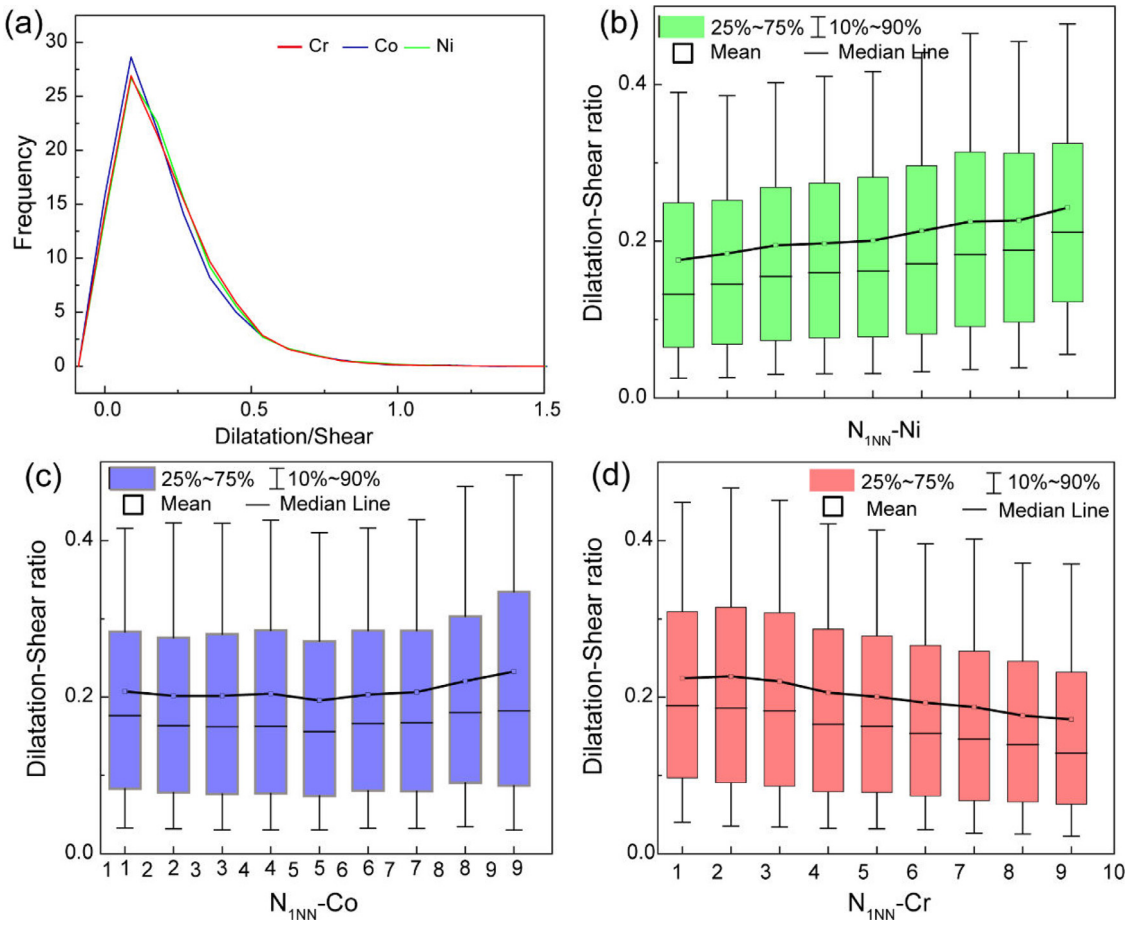

Fig. 12. Dependence of dilatation-shear ratio on their atomic environments of chemical disordered GBs. (a) Dilatation-shear ratio distribution for different elements, (b–d) variation of dilatation-shear ratio with the number of Co, Cr and Ni in the first-nearest-neighbor shell within a radius of 3 Å. The statistical data are collected from the atomic properties at strain ε<7% in all chemical disordered GBs including R-K, R-FK and R-PM GBs. The black lines indicate the change in average dilatation-shear ratio as a function of the N_{1NN} atomic number.

To explore how the inhomogeneous chemical distributions affect GB fracture resistance, we systematically analyze the dependence of atomic dilatation-shear ratio on their local chemical environment. The results are shown in Fig. 12, where the statistical data are collected from the atomic chemical and kinematical properties at strain ε<7% in all the chemical disordered GBs. As shown in Fig. 12(a), there is no significant difference in the atomic dilatation-shear ratio between the principal elements of Co, Cr and Ni, suggesting that the atomic deformation kinematics are insensitive to the element type. It is expected that the dilatation-shear ratio should depend on the local chemical environment governing the energy landscapes for atomic deformation.

Fig. 12(b–d) shows the dependence of dilatation-shear ratio of GB atoms on their neighbors. As seen, the dilatation-shear ratio increases with the number of nearest Co and Ni neighbors, while it decreases continuously with the number of nearest Cr atoms. This suggests that voids or cracks are more prone to nucleation and growth in Ni- or Co-rich regions, while Cr-rich sites contribute to the inhibition of crack formation and propagation. A similar result that voids prefer to nucleate in Ni rich environment was found in a CrCoNi HEA after shock simulations [85]. Our previous first principle study has shown that the structural relaxation induced atomic shear strain increases with the number of surrounding Cr atoms, for which Cr-containing chemical bonds exhibit drastic structure distortion [45]. This suggests that the atoms in Cr-rich environments tend to shear deform to reconcile the severe interatomic bond distortions, leading to a lower dilatation-shear ratio that prevents the formation of voids and cracks. In this light, the excellent fracture resistance of chemical disordered GBs may be connected to the bonding distortions, which would be highlighted by the presence of Cr.

The dependence of dilatation-shear ratio on their local chemical environment, summarized in Fig. 12, provides quantitative evidence for the chemical dependence of GB atomic kinematics and hence the GB fracture behavior. To explore the underlying mechanism responsible for this chemistry dependence, the electronic behavior of GB atoms is analyzed in terms of their electronic distribution and charge transfer during deformation. The charge transfer analysis reveals a significant positive correlation (with a correlation coefficient of 0.55) between transferred charge (ΔQ) and shear strain, as shown in Fig. 13(a). This indicates that the atomic deformation is related to the local electron redistribution. Specifically, it highlights the role of charge transfer on shear deformation that avails to reduce dilatation-shear ratio. Similar observation was also found in metallic glass, in which increased charge transfer contributes to the softening of shear modulus [86]. Moreover, detailed analysis of the electronic structures in several BCC transition metals and alloys shows that the potential for shear deformation can be enhanced through Jahn-Teller distortion [87]. As demonstrated by Qi and Chrzan [87], if there are partially occupied and symmetry-related degenerate orbitals near the Fermi level, the bonding will deform to break this symmetry and thereby split the degenerate orbitals to lower the total energy of the alloy. The same concept has been used to explain the BCC-BCT-FCC transition for

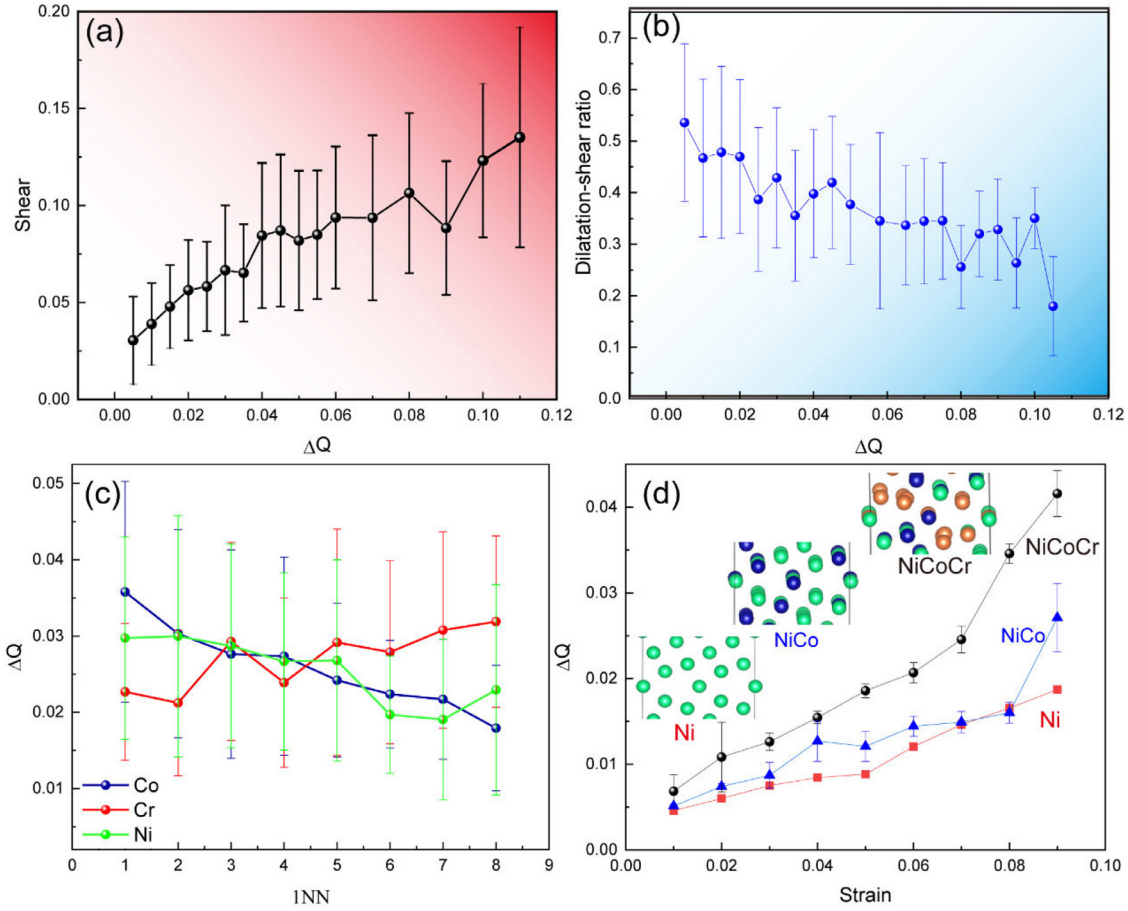

Fig. 13. (a) Correlation between atomic shear strain and change in atomic charge. (b) Correlation between atomic dilatation-shear ratio and change in atomic charge. (c) Effects of the 1 nn atomic numbers of various elements on the charge transfer in CoCrNi GB. (d) Evolution of charge transfer as strain in CrCoNi GB and pure Ni GB.

transition metals, where phase transition has been found to depend on the number of electrons whose variation can shift the Fermi energy level [88].

In this study, charge transfer increases the driving force for the Jahn-Teller distortion by shifting the local Fermi level, which increases the population of symmetry-equivalent orbitals close to Fermi level. The breaking of symmetry during the Jahn-Teller distortion induces preferential shear deformation instead of volume dilatation, resulting in a lower dilatation-shear ratio, as demonstrated in Fig. 13(b). Fig. 13(c) shows the atomic charge transfer as a function of local chemical environment. As shown, the transferred charge (ΔQ) increases with the neighboring Cr atoms and decreases with Ni and Co, which is opposite to that of dilatation-shear ratio shown in Fig. 12. The electronic shells of Ni and Co are nearly saturated and difficult to gain or lose electrons, while the d-band of Cr is only partially filled and tends to transfer charge to form covalent bonds. The lower dilatation-shear ratio in the Cr-rich environment suggests that the atoms within a flexible electron environment tend to shear deformation and favor reducing the dilatation-shear ratio.

The results illustrated in Fig. 13(a–c) suggest that the substantial charge transfer in Cr-rich environment contributes to the inhibition of void formation by enhancing shear deformation through the Jahn-Teller distortion. The significant difference in the fracture mode between pseudo-element GBs and chemical disordered GBs may originate from the difference in their electron redistribution capabilities. Evidence for this is that the transferred charge in pure Ni and random NiCo is significantly less than that in random CrCoNi GB under the same axial strain, as shown in Fig. 13(d). For pure Ni GB, the atoms possess a homogeneous electronic structure with a nearly full d-band, suggesting limited electron redistribution capability. A similar situation would also appear in the pseudo-element GBs which possess a homogeneous chemistry, even though the d-band would be underfilled by considering the hypothetical averaging of atomic natures of Ni, Co and Cr. In contrast, the inhomogeneous atomic distribution in chemical disordered GBs leads to a fluctuant electron distribution that is prone to transfer atomic charge during deformation. Particularly, the randomly distributed Cr atoms with partially filled d-shell and thus larger electronic flexibility can serve as a medium to enhance the charge transfer [89], as manifested by the stronger electron redistribution ability of CrCoNi GB than random NiCo GB. The stronger charge redistribution ability of chemical disordered CrCoNi GBs enhances shear deformation through Jahn-Teller distortion, which lowers the dilatation-shear ratio and thus prevents void formation and GB fracture.

Beyond the present analysis, the prospect of chemical disorder preventing GB crack formation and propagation raises another interesting question as to whether chemical order or composition dominates this. Recall that the atoms within Cr-rich environments exhibit shear-dominated deformations with a low dilatation-shear ratio due to the electronic flexibility of Cr, suggesting a constructive role of Cr in preventing void formation. In this regard, sufficient Cr content within GB is required to ensure an adequate charge redistribution capacity that facilitates shear deformation and hence prevents cracking. To prove this, additional MD tension tests were performed on several bi-crystals with different compositions involving pure Ni, chemical disor-

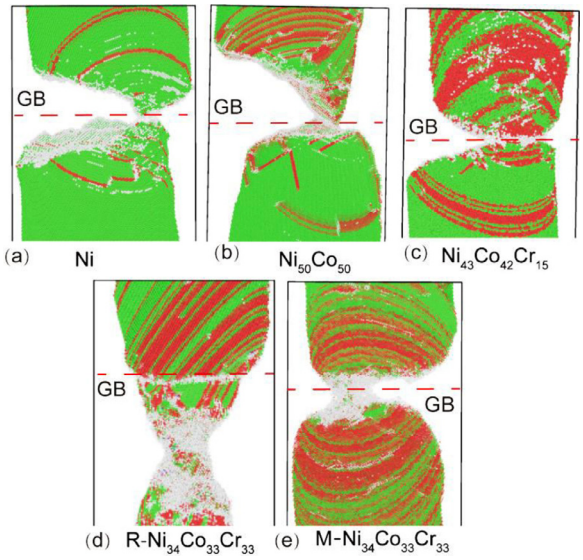

Fig. 14. Tension bi-crystal atomic structure before fracture showing different fracture modes in Ni and Ni-based HEAs. (a) Ni, (b) NiCo, (c) $Ni_{43}Co_{42}Cr_{15}$, (d) CrCoNi with random chemical distribution. (e) CrCoNi with pronounced local chemical order.

dered NiCo and $Ni_{43}Co_{42}Cr_{15}$, the results are shown in Fig. 14. As shown, the GBs with few Cr or non-Cr tend to fracture through cracking. It also shows that the amount of dislocation in the crack surface increases with Cr content with the order of Ni<NiCo<$Ni_{43}Co_{42}Cr_{15}$<$Ni_{34}Co_{33}Cr_{33}$, suggesting an increasing plastic deformation with Cr content and degree of disorder.

With respect to the local chemical order, for which the presence, nature, and effects are all topics of current interest and debate, a moderate charge redistribution ability and thus a moderate resistance to void/crack and fracture is expected. As shown in Fig. 14(e), the CrCoNi bi-crystal with pronounced local chemical order (called clustered GB, see details in our previous study [45]) also exhibits a typical crack induced GB fracture behavior under tension loading. Clustered Ni and preferred Co-Cr bonding in this clustered GB limits the electron redistribution and thus reduces the atomic deformation compatibility during deformation, leading to cracking and fracture. This provides a possible atomic-scale explanation for the experimentally observed grain boundary cracking in the homologous CrMnFeCoNi HEAs with the nano-clustering of Ni and Cr separately [41]. Comparing chemical disordered GBs and clustered GBs with the same composition suggests that the disordered GB chemistry is one of the necessary conditions to ensure GB fracture resistance.

Based on the above analysis, it can be concluded that not only disordered chemical distribution but also sufficient “harmonic elements” possessing large electronic flexibility contribute to improving the GB fracture resistance. Even if the analysis focuses only on CrCoNi MEAs, we envision that both H/MEAs and traditional alloys can achieve strong GB fracture resistance by enhancing the electron redistribution ability through elaborate alloying addition and manufacturing method. In this study, the excellent GB deformability and fracture resistance of chemical disordered CrCoNi GBs may result from their strong charge redistribution ability which primarily originates from the partially filled d-shells of Cr. This could also be another factor, besides the outstanding strain hardening ability, responsible for the exceptional damage tolerance of CrCoNi MEA and CrCoNiFeMn HEA [53,54,79]. Similar elements with partially filled d-shells, such as Fe, Mn, Mo and Zr should also play a positive role in impeding GB fracture. For example, the significant improvement of ductility in nanocrystalline Cu by introducing Cu-Zr amorphous intergranular films via Zr segregation [2] may benefit from the partially filled d states of Zr. This agreement is reassuring and provides a chemical understanding of the GB fracture behavior, yielding a new strategy for the design of high-performance materials with enhanced GB fracture resistance.

4. Conclusions

The chemical inhomogeneity effects are evaluated for Σ17(140)[001], Σ29(730)[001] and Σ5(210)[001] symmetric tilt GBs. We have further studied the atomic and electronic level pathway and mechanism for GB deformation and fracture in the model CrCoNi alloys, by taking Σ5 (210) STGB as a representative. The following conclusions can be drawn from this work:

(1) Inhomogeneity chemical distribution inhibits GB fracture effectively for the considered high angle GBs. The GBs with disordered chemical distribution show excellent fracture resistance, regardless of their atomic topology configuration and misorientation. Whereas the corresponding pseudo-element GBs, which bear the same bulk properties of equiatomic CrCoNi MEA but no chemical fluctuation, are prone to fracture via crack initiation and propagation along GB.
(2) GB atomic deformation kinematics, which plays a pivotal role in the fracture resistance, depends largely on GB chemical distribution. The dilatation-shear ratio that characterizes the relative degree of atomic shear deformation and dilatation in chemical disordered GBs is much lower than that of pseudo-element GBs.
(3) Not only disordered chemical distribution but also sufficient “harmonic elements” with large electronic flexibility contribute to improving the GB fracture resistance. First principle electronic behavior analysis reveals that the stronger charge redistribution ability of chemical disordered CrCoNi GBs enhances shear deformation through Jahn-Teller distortion and thus prevents crack formation and GB fracture. Their strong charge redistribution ability is the result of adequate Cr atom with partially filled d-shells in cooperation with the disordered GB chemistry.

Acknowledgments

This work is financially supported by the National Natural Science Foundation of China (NSFC) (Nos. 12102433, U2241285, 11972346 and U2141204), the NSFC Basic Science Center Program for "Multi-scale Problems in Nonlinear Mechanics" (No. 11988102), the Key Research Program of the Chinese Academy of Sciences (No. ZDRW-CN-2021-2-3).

References

[1] Y.M. Wang, K. Wang, D. Pan, K. Lu, K.J. Hemker, E. Ma, Scr. Mater. 48 (2003) 1581–1586.
[2] A. Khalajhedayati, Z. Pan, T.J. Rupert, Nat. Commun. 7 (2016) 10802.
[3] D. Farkas, H. Van Swygenhoven, P.M. Derlet, Phys. Rev. B 66 (2002) 601011–601014.
[4] Z. Gao, Y. Zhao, J.M. Park, A.H. Jeon, K. Murakami, S.-I. Komazaki, K. Tsuchiya, U. Ramamurty, J.-I. Jang, Scr. Mater. 210 (2022) 114472.
[5] Z. Pan, T.J. Rupert, Comput. Mater. Sci. 93 (2014) 206–209.
[6] S. Chandra, N. Naveen Kumar, M.K. Samal, V.M. Chavan, S. Raghunathan, Comput. Mater. Sci. 130 (2017) 268–281.
[7] D.V. Bachurin, Int. J. Fract. 214 (2018) 69–78.
[8] J.S. Weaver, N. Li, N.A. Mara, D.R. Jones, H. Cho, C.A. Bronkhorst, S.J. Fensin, G.T. Gray, Acta Mater. 156 (2018) 356–368.
[9] G. Dehm, B.N. Jaya, R. Raghavan, C. Kirchlechner, Acta Mater. 142 (2018) 248–282.
[10] S. Sun, Y. Yang, C. Han, G. Sun, Y. Chen, H. Zong, J. Hu, S. Han, X. Liao, X. Ding, J. Lian, J. Mater. Sci. Technol. 127 (2022) 98–107.
[11] Z. Jiao, G.S. Was, J. Nucl. Mater. 408 (2011) 246–256.
[12] W. Xu, Y.C. Xin, B. Zhang, X.Y. Li, Y.C. Xin, B. Zhang, X.Y. Li, Acta Mater. 225 (2021) 117607.
[13] X. Dong, N. Li, Y. Zhou, H. Peng, Y. Qu, Q. Sun, H. Shi, R. Li, S. Xu, J. Yan, J. Mater. Sci. Technol. 93 (2021) 244–253.

[14] M.D. Sangid, H.J. Maier, H. Sehitoglu, Int. J. Plast. 27 (2011) 801–821.
[15] W. Li, S. Chen, P.K. Liaw, Scr. Mater. 187 (2020) 68–75.
[16] J.R. Rice, J. Wang, Mater. Sci. Eng. A 107 (1989) 23–40.
[17] T. Hu, S. Yang, N. Zhou, Y. Zhang, J. Luo, Nat. Commun. 9 (2018) 2764.
[18] A. Tehranchi, W.A. Curtin, J. Mech. Phys. Solids 101 (2017) 150–165.
[19] J. Luo, H. Cheng, K.M. Asl, C.J. Kiely, M.P. Harmer, Science 333 (2011) 1730–1734.
[20] H. Zhao, P. Chakraborty, D. Ponge, T. Hickel, B. Sun, C.H. Wu, B. Gault, D. Raabe, Nature 602 (2022) 437–441.
[21] W. Li, P.K. Liaw, Y. Gao, Intermetallics 99 (2018) 69–83.
[22] Z. Xue, X. Zhang, J. Qin, M. Ma, R. Liu, J. Mater. Sci. Technol. 36 (2020) 140–148.
[23] P.G. Christodoulou, S. Dancette, R.A. Lebensohn, E. Maire, I.J. Beyerlein, Int. J. Plast. 147 (2021) 103104.
[24] S. Zhang, L. Wang, G. Zhu, M. Diehl, A. Maldar, X. Shang, X. Zeng, Int. J. Plast. 150 (2022) 103186.
[25] D. Farkas, R. Nogueira, M. Ruda, B. Hyde, Metall. Mater. Trans. A 36 (2005) 2067–2072.
[26] Y. Ding, H. Yu, K. Zhao, M. Lin, S. Xiao, M. Ortiz, J. He, Z. Zhang, Scr. Mater. 204 (2021) 114122.
[27] K. Leitner, D. Scheiber, S. Jakob, S. Primig, H. Clemens, E. Povoden-Karadeniz, L. Romaner, Mater. Des. 142 (2018) 36–43.
[28] F.Z. Dai, B. Wen, Y. Sun, Y. Ren, H. Xiang, Y. Zhou, J. Mater. Sci. Technol. 123 (2022) 26–33.
[29] A.R. Krause, P.R. Cantwell, C.J. Marvel, C. Compson, J.M. Rickman, M.P. Harmer, J. Am. Ceram. Soc. 102 (2018) 778–800.
[30] P.R. Cantwell, T. Frolov, T.J. Rupert, A.R. Krause, C.J. Marvel, G.S. Rohrer, J.M. Rickman, M.P. Harmer, Ann. Rev. Mater. Res. 50 (2020) 465–492.
[31] S. Liang, M. Huang, L. Zhao, Y. Zhu, Z. Li, Int. J. Plast. 143 (2021) 103023.
[32] Y. Cheng, Z.H. Jin, Y.W. Zhang, H. Gao, Acta Mater. 58 (2010) 2293–2299.
[33] T. Shimokawa, M. Tsuboi, Acta Mater. 87 (2015) 233–247.
[34] J.J. Möller, E. Bitzek, Acta Mater. 73 (2014) 1–11.
[35] Y. Wang, J. Li, A.V. Hamza, T.W. Barbee, Proc. Natl. Acad. Sci. U. S. A. 104 (2007) 11155–11160.
[36] C. Brandl, T.C. Germann, A. Misra, Acta Mater. 61 (2013) 3600–3611.
[37] Z. Pan, T.J. Rupert, Acta Mater. 89 (2015) 205–214.
[38] B. Wei, W. Wu, D. Xie, M. Nastasi, J. Wang, Acta Mater. 212 (2021) 116918.
[39] P. Li, L. Wang, S. Yan, M. Meng, Y. Zhou, K. Xue, Int. J. Refract. Met. Hard Mater. 94 (2021) 105376.
[40] N. Zhou, T. Hu, J. Luo, Curr. Opin. Solid State Mater. Sci. 20 (2016) 268–277.
[41] K. Ming, L. Li, Z. Li, X. Bi, J. Wang, Sci. Adv. 5 (2019) 0639.
[42] L. Li, Z. Li, A. Kwiatkowski da Silva, Z. Peng, H. Zhao, B. Gault, D. Raabe, Acta Mater. 178 (2019) 1–9.
[43] T. Yang, Y.L. Zhao, W.P. Li, C.Y. Yu, J.H. Luan, D.Y. Lin, L. Fan, Z.B. Jiao, W.H. Liu, X.J. Liu, J.J. Kai, J.C. Huang, C.T. Liu, Science 432 (2020) 427–432.
[44] Q. Ding, Y. Zhang, X. Chen, X. Fu, D. Chen, S. Chen, L. Gu, F. Wei, H. Bei, Y. Gao, M. Wen, J. Li, Z. Zhang, T. Zhu, R.O. Ritchie, Q. Yu, Nature 574 (2019) 223–227.
[45] F. Cao, Y. Chen, S. Zhao, E. Ma, L. Dai, Acta Mater. 209 (2021) 116786.
[46] S. Chen, Z.H. Aitken, S. Pattamatta, Z. Wu, Z.G. Yu, R. Banerjee, D.J. Srolovitz, P.K. Liaw, Y.W. Zhang, Acta Mater. 206 (2021) 116638.
[47] V. Yamakov, E. Saether, D.R. Phillips, E.H. Glaessgen, J. Mater. Sci. 42 (2007) 1466–1476.
[48] V. Yamakov, E. Saether, D.R. Phillips, E.H. Glaessgen, J. Mech. Phys. Solids 54 (2006) 1899–1928.
[49] P. Gao, Z. Ma, J. Gu, S. Ni, T. Suo, Y. Li, M. Song, Y.W. Mai, X. Liao, Sci. Chin. Mater. 65 (2022) 811–819.
[50] Q. Huang, Q. Zhao, H. Zhou, W. Yang, Int. J. Plast. 159 (2022) 103466.
[51] P. Garg, T.J. Rupert, Acta Mater. 244 (2022) 118599.
[52] S. Chen, H.S. Oh, B. Gludovatz, S.J. Kim, E.S. Park, Z. Zhang, R.O. Ritchie, Q. Yu, Nat. Commun. 11 (2020) 826.
[53] B. Gludovatz, A. Hohenwarter, K.V. Thurston, H. Bei, Z. Wu, E.P. George, R.O. Ritchie, Nat. Commun. 7 (2016) 10602.
[54] B. Gludovatz, A. Hohenwarter, D. Catoor, E.H. Chang, E.P. George, R.O. Ritchie, Science 345 (2014) 1153–1158.
[55] M. Naeem, H. Zhou, H. He, S. Harjo, T. Kawasaki, S. Lan, Z. Wu, Y. Zhu, X.L. Wang, Appl. Phys. Lett. 119 (2021) 131901.
[56] W.R. Jian, Z. Xie, S. Xu, Y. Su, X. Yao, I.J. Beyerlein, Acta Mater. 199 (2020) 352–369.
[57] P. Wang, S. Xu, J. Liu, X. Li, Y. Wei, H. Wang, H. Gao, W. Yang, J. Mech. Phys. Solids 98 (2017) 290–308.
[58] S. Plimpton, J. Comput. Phys. 117 (1995) 1–19.
[59] Q.-J. Li, H. Sheng, E. Ma, Nat. Commun. 10 (2019) 3563.
[60] P.M. Larsen, S. Schmidt, J. Schiøtz, Modelling Simul. Mater. Sci. Eng. 24 (2016) 55007.
[61] A. Stukowski, Modelling Simul. Mater. Sci. Eng. 18 (2010) 015012.
[62] L.B. Freund, Dynamic Fracture Mechanics, Cambridge Monographs On Mechanics and Applied Mathematics, Cambridge University Press, Cambridge, 1990.
[63] G. Kresse, J. Furthmüller, Comput. Mater. Sci. 6 (1996) 15–50.
[64] A. van de Walle, P. Tiwary, M. de Jong, D.L. Olmsted, M. Asta, A. Dick, D. Shin, Y. Wang, L.Q. Chen, Z.K. Liu, Calphad 42 (2013) 13–18.
[65] D. Roundy, C.R. Krenn, M.L. Cohen, J.W. Morris Jr, Phys. Rev. Lett. 82 (1999) 2713.
[66] J.P. Perdew, K. Burke, M. Ernzerhof, Phys. Rev. Lett. 77 (1996) 3865.
[67] P.E. Blöchl, Phys. Rev. B 50 (1994) 17953–17979.
[68] D. Utt, A. Stukowski, K. Albe, Acta Mater. 186 (2020) 11–19.
[69] D. Farkas, J. Mater. Sci. 55 (2020) 9173–9183.
[70] B. Kuhr, D. Farkas, I.M. Robertson, D. Johnson, G. Was, Metall. Mater. Trans. A51 (2020) 667–683.
[71] D.C. Johnson, B. Kuhr, D. Farkas, G.S. Was, Acta Mater. 170 (2019) 166–175.
[72] X.W. Gu, M. Jafary-Zadeh, D.Z. Chen, Z. Wu, Y.W. Zhang, D.J. Srolovitz, J.R. Greer, Nano Lett. 14 (2014) 5858–5864.
[73] P. Murali, T.F. Guo, Y.W. Zhang, R. Narasimhan, Y. Li, H.J. Gao, Phys. Rev. Lett. 107 (2011) 215501.
[74] E. Martínez-Pañeda, S. Del Busto, C.F. Niordson, C. Betegón, Int. J. Hydrogen Energy 41 (2016) 10265–10274.
[75] Y. Lou, P. Wu, C. Zhang, J. Wang, X. Li, R. Chai, J.W. Yoon, Int. J. Solids Struct. 256 (2022) 111993.
[76] P. Andric, W.A. Curtin, Modelling Simul. Mater. Sci. Eng. 27 (2019) 013001.
[77] A. Tehranchi, W.A. Curtin, Modelling Simul. Mater. Sci. Eng. 25 (2017) 075013.
[78] J.R. Rice, J. Mech. Phys. Solids 40 (1992) 239–271.
[79] J. Li, H. Chen, Q. He, Q. Fang, B. Liu, C. Jiang, Y. Liu, Y. Yang, P.K. Liaw, Phys. Rev. Mater. 4 (2020) 103612.
[80] H. Wang, D. Chen, X. An, Y. Zhang, S. Sun, Y. Tian, Z. Zhang, A. Wang, J. Liu, M. Song, S.P. Ringer, T. Zhu, X. Liao, Sci. Adv. 7 (2021) eabe3105.
[81] E. Martínez-Pañeda, V.S. Deshpande, C.F. Niordson, N.A. Fleck, J. Mech. Phys. Solids 126 (2019) 136–150.
[82] J.A. Zimmerman, C.L. Kelchner, P.A. Klein, J.C. Hamilton, S.M. Foiles, Phys. Rev. Lett. 87 (2001) 165507.
[83] Z.-Y. Yang, Y.-J. Wang, L.-H. Dai, Phys. Rev. Res. 4 (2022) 23220.
[84] Y.J. Wang, M.Q. Jiang, Z.L. Tian, L.H. Dai, Scr. Mater. 112 (2016) 37–41.
[85] Z. Xie, W.R. Jian, S. Xu, I.J. Beyerlein, X. Zhang, Z. Wang, X. Yao, Acta Mater. 221 (2021) 117380.
[86] I. Lobzenko, Y. Shiihara, T. Iwashita, T. Egami, Phys. Rev. Lett. 124 (2020) 085503.
[87] L. Qi, D.C. Chrzan, Phys. Rev. Lett. 112 (2014) 1–5.
[88] S. Lee, R. Hoffmann, J. Am. Chem. Soc. 124 (2002) 4811–4823.
[89] S. Zhao, T. Egami, G.M. Stocks, Y. Zhang, Phys. Rev. Mater. 2 (2018) 013602.